# High-throughput label-free detection of DNA-to-RNA transcription inhibition using brightfield microscopy and deep neural networks

Allan Sauvat, Giulia Cerrato, Juliette Humeau, Marion Leduc, Oliver Kepp, Guido Kroemer

Computers in Biology and Medicine 133 (2021) 104371

Contents lists available at ScienceDirect

Computers in Biology and Medicine

journal homepage: http://www.elsevier.com/locate/compbiomed

# High-throughput label-free detection of DNA-to-RNA transcription inhibition using brightfield microscopy and deep neural networks

Allan Sauvat [a,b,*], Giulia Cerrato [a,b,c], Juliette Humeau [a,b], Marion Leduc [a,b], Oliver Kepp [a,b], Guido Kroemer [a,b,d,e,f]

[a] Centre de Recherche des Cordeliers, Equipe labellisée par la Ligue contre le Cancer, Université de Paris, Sorbonne Université, Inserm U1138, Institut Universitaire de France, Paris, France
[b] Metabolomics and Cell Biology Platforms, Gustave Roussy Cancer Center, Villejuif, France
[c] Faculty of Medicine, Université Paris Saclay, Kremlin-Bicêtre, France
[d] Suzhou Institute for Systems Medicine, Chinese Academy of Medical Sciences, Suzhou, China
[e] Poˆle de Biologie, Hoˆpital Européen Georges Pompidou, AP-HP, Paris, France
[f] Karolinska Institutet, Department of Women's and Children's Health, Karolinska University Hospital, Stockholm, Sweden

ARTICLE INFO

*Keywords:*
Transmitted light microscopy
Immunogenic cell death
Cellular imaging
Systems biology
Convolutional neural network
Semantic segmentation
UNET

ABSTRACT

Drug discovery is in constant evolution and major advances have led to the development of *in vitro* high-throughput technologies, facilitating the rapid assessment of cellular phenotypes. One such phenotype is immunogenic cell death, which occurs partly as a consequence of inhibited RNA synthesis. Automated cell-imaging offers the possibility of combining high-throughput with high-content data acquisition through the simultaneous computation of a multitude of cellular features. Usually, such features are extracted from fluorescence images, hence requiring labeling of the cells using dyes with possible cytotoxic and phototoxic side effects. Recently, deep learning approaches have allowed the analysis of images obtained by brightfield microscopy, a technique that was for long underexploited, with the great advantage of avoiding any major interference with cellular physiology or stimulatory compounds. Here, we describe a label-free image-based high-throughput workflow that accurately detects the inhibition of DNA-to-RNA transcription. This is achieved by combining two successive deep convolutional neural networks, allowing (1) to automatically detect cellular nuclei (thus enabling monitoring of cell death) and (2) to classify the extracted nuclear images in a binary fashion. This analytical pipeline is R-based and can be easily applied to any microscopic platform.

## 1. Introduction

Immunogenic cell death (ICD) is a peculiar type of cell death that can trigger specific immune responses in the context of anticancer treatment. Such an event can be induced in cancer cells by different means, including anthracyclines-based chemotherapy or radiotherapy, which were both shown to improve prognosis in several clinical contexts [1]. However, the long-term use of these treatments can cause severe and possibly lethal side-effects, notably irreversible cardiotoxicity [2] and therapy-related malignancies, thus limiting their clinical application. The link between side effects and therapeutic efficacy remains unclear and there is an emerging need of discovering novel ICD inducers endowed with the capacity to elicit efficient anticancer immune response while limiting collateral damage. Thus far, the discovery of novel ICD inducers relied on screening compounds libraries for their capacity to induce multi-molecular signatures of immunogenicity in cultured cells. Such signs of immunogenicity include the release of ATP, high mobility group protein B1 and annexin A1 from cells, as well as the exposure of calreticulin and heat shock proteins on their plasma membrane surface [3], resulting in an expensive and time-consuming process.

Recently, we identified dactinomycin (DACT), a well-known inhibitor of DNA-to-RNA transcription [4,5], as a novel ICD inducer, and subsequent mechanistic studies unraveled that this transcriptional inhibition is an important shared feature among ICD-stimulatory compounds [6]. Transcription is a highly-regulated mechanism occurring in the nucleus and catalyzed by RNA polymerases, through which coding and non-coding RNA are synthesized. It is divided into four subsequent

* Corresponding author. UMR1138 équipe 11, Centre de Recherche des Cordeliers, 15 Rue de l'École de Médecine, 75006, Paris, France.
*E-mail address:* allan.sauvat@gustaveroussy.fr (A. Sauvat).

https://doi.org/10.1016/j.compbiomed.2021.104371
Received 23 November 2020; Received in revised form 30 March 2021; Accepted 30 March 2021
Available online 4 April 2021

steps: pre-initiation complex formation, transcription initiation, elongation and termination. Several anticancer agents target transcription, most of them affecting mainly three of the four cited steps, DACT preventing the elongation process [5,7]). However, the finding that anticancer agents that inhibit transcription are better ICD inducers than anticancer drugs that fail to do so has marked a hiatus in the field. In substance, for the identification of new ICD inducer, it is sufficient to screen drug libraries for transcriptional inhibitors. Still, identifying such inhibitors would require the implementation of relatively expensive workflows, one of the common methods consisting in the assessment of the colocalization between nucleolin and fibrillarin by immunofluorescence. The separation of these two proteins is a sign of transcriptional inhibition [8] and is linked to changes in the morphology of nucleoli, the major sites of transcription in the nucleus, which can be discerned by transmitted light microscopy. However, such changes in nucleolar morphology are hardly exploitable in a standard automated fashion due to the signal complexity of brightfield images [9].

Recent advances in machine learning may facilitate the exploitation of such complex images, notably thanks to the development of deep convolutional neural networks (DCNN) that outperformed traditional image analysis algorithms [10]. Two common applications of the aforementioned networks are image classification and semantic segmentation. In the first, a series of convolutions allows to encode non-linear features that are used to predict the class of an image, while in the second, features are decoded to generate a pixelwise classification, enabling the precise detection of objects. However, DCNNs are not yet broadly applied to medical imaging (radiology), let alone cell imaging (microscopy) [11–13]. Nonetheless, several common structures were successfully adapted to cell biology: the VGG16 network, that achieved 92.7% top-5 test accuracy in ImageNet [14], notably allowed to recognize drug resistance in cancer cell cultures [15]. In the same manner, the UNET model was auspiciously used to predict two- and three-dimensional cellular component objects from label-free brightfield micrographs and electronographs [16–18].

Here, we describe a simple label-free image-based workflow for the evaluation of immunogenicity, allowing to detect both the level of transcription inhibition and the viability of cancer cell populations by means of a dual deep-learning model. This process consists in (1) detecting precise nuclear regions in brightfield and then (2) extracting and classifying identified nuclei into distinct phenotypic classes.

## 2. Material and methods

### 2.1. Cell culture and reagents

Human osteosarcoma U2OS, human brain neuroglioma H4, mouse colon carcinoma CT26, mouse embryonic fibroblast MEF and mouse fibrosarcoma MCA205 cells were routinely maintained at 37 °C, 5% $CO_2$ in a humidified environment, cultured in Dulbecco's modified Eagle's medium (Thermo Fisher Scientific, Carlsbad, CA, USA) supplemented with 10% fetal bovine serum (Gibco® by Thermo Fisher Scientific) and 1% HEPES (Thermo Fisher Scientific). Oleate was furnished by Larodan (Solna, Sweden) and all the other compounds were purchased from Sigma Aldrich (Saint-Louis, MO, USA).

### 2.2. Fluorescence microscopy and image acquisition

U2OS, H4, CT26, MEF and MCA205 cells were seeded in 96-well μClear imaging plates (Greiner-bio-one, Kremsmünster, Austria) and allowed to adhere for 24 h (37 °C, 5% $CO_2$ atmosphere). The next day, cells were left untreated (complete medium, CM) or treated with 500 μM oleate (OL), 0.1% dimethylsulfoxyde (solvent control, DMSO), 1 μM DACT, 4 μM mitoxantrone (MTX), 150 and 500 μM oxaliplatin (OXA), 2 μM staurosporine (STS), as well as 150 and 500 μM cisplatin (CDDP) for 4 h or 16 h. After treatment, cells were either fixed and stained in a 3.7% paraformaldehyde (PFA) solution containing 10 μg/mL Hoechst 33342 for 20 min at room temperature, and thereafter rinsed twice with phosphate buffered saline (PBS), or left unstained for imaging. Images (at least three viewfields per well) were acquired on an ImageXpress confocal automated microscope (Molecular Devices, San Jose, CA, USA) using a CFI PlanApo Lambda 20× objective (Nikon, Tokyo, Japan) with a numerical aperture of 0.75.

### 2.3. Image storage and compression

Images acquired on the ImageXpress Confocal automated bioimager were stored as uncompressed MetaMorph 7.5 TIFF files with a pixel depth of 16 bits and a resolution of 5 megapixels (2048 × 2048 pixel matrix). Pixel size was 350 nm along both x and y axes.

### 2.4. Training set preparation for label-free nuclei detection

Six independent acquisitions featuring human and mouse cells treated with compounds inducing various cellular stresses (CM as control, DACT as transcription inhibitor, STS as apoptosis inducer, OL as integrated stress response inducer), were performed using BLUE and TL channels, capturing Hoechst 33342 nuclear staining and transmitted light respectively. In total, 296 × 2 images (publicly available at https://doi.org/10.6084/m9.figshare.c.5205278.v2) were acquired and processed as described below (Fig. 1, Fig. 2, Fig. 4). All processing steps were performed in R using the *EBImage* [19], *RBioFormats* (https://github.com/aoles/RBioFormats), *MetaxpR* (https://github.com/asauvat/MetaxpR) and *MorphR* (https://github.com/kroemerlab/MorphR) packages. First, images were normalized plate-wise using their internal control's pixel intensity distribution, *i.e.* image histograms were scaled between its 0.0005% and 99.9995% intensity quantiles. Normalized BLUE images were then scaled following a sigmoid transformation, defined as follows:

$$I_n = \frac{1}{e^{-\lambda(I_r - z)}} \quad (1)$$

where $I_n$ corresponds to the normalized pixel intensity, $I_r$ to the raw intensity, $\lambda$ to the parameter controlling transformation smoothness and z to the center of the transformation. For an optimal object segmentation, parameters were defined as $\lambda = 0.001$ and $z = 0.05$. The resulting image was thereafter binarized using a threshold computed with Otsu's method [20]. Then, the obtained mask was cleaned by three successive morphologic operations: (1) an opening with a disc kernel of size 5, (2) a closing with a disc kernel of size 3, and (3) a geodesic opening with a disc kernel of size 23. Finally, masks, as well as normalized TL images, were untiled into blocks of 256 × 256 pixels, thus resulting in 2 tensors $t_{mask}(18944, 256, 256, 1)$ and $t_{brightfield}(18944, 256, 256, 1)$ to be fed to the UNET model. Details about tensors composition can be consulted in the Supplementary Table S3.

### 2.5. UNET training for label-free nuclei detection

A 3-layer UNET model [16] was generated using the Google *Tensorflow* framework [21] by means of *tensorflow*, *keras* (https://cran.r-project.org/) and *unet* (https://github.com/r-tensorflow/unet) R packages. The detailed network architecture is shown in Fig. 2. Two other networks, FCN8 [22] and SEGNET-BASIC [23], were implemented and trained for performance benchmarks. The input data were randomly split into "training" and "validation" sets following several ratios, either patch-wise or image-wise, and the different models were trained using an *Adam optimizer* [24], the evaluation metrics being represented by both *accuracy* and *Dice coefficient*, defined as:

$$D = \frac{2(P_P \cap P_T)}{P_P \cup P_T} \quad (2)$$

Where $P_P$ corresponds to the predicted object pixels, $P_T$ to the ground

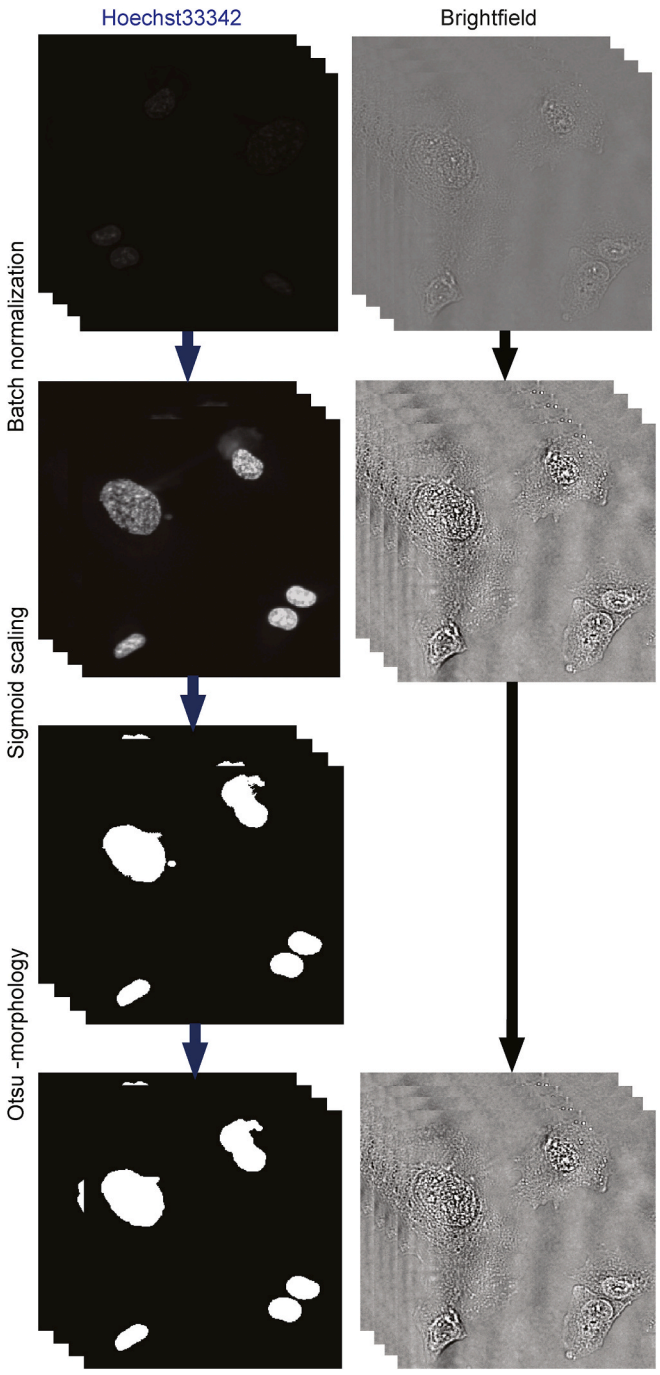


**Fig. 1.** Preparation of training set for label-free nuclei detection. The main processing steps are reported in a hierarchical diagram. After automated acquisition of Hoechst 33342 fluorescence (BLUE channel) and brightfield images (TL channel), images are batch-normalized plate-wise according to pixel percentiles in control images. Nuclear masks are computed after applying a sigmoid scaling to Hoechst 33342 normalized images, using the Otsu's method. The obtained masks are cleaned by applying successive opening and closing operations with a 5-pixel and a 3-pixel-sized disc-shaped kernels respectively, followed by a geodesic opening with a disc kernel of radius 23.

truth object pixels, and *D* the Dice coefficient. The *loss* was defined as the sum of *binary cross-entropy* (BCE) and *1-D* (Dice inverse). Altogether the obtained trained networks output a nuclear probability map from brightfield image patches.

### 2.6. UNET performance evaluation

Two independent acquisitions (varying treatment dose and incubation time, as indicated in Table S4) were performed with the same settings as used for establishing the training set, yielding 2 × 592 images (BLUE and TL channels) including 208 micrographs of U2OS cells, and 96 of each other cell type. BLUE images were processed as previously described to generate nuclear masks and were then used as a reference for evaluating the deep-learning-based segmentation of TL images, after calculating the number of cells (as reported in Table S4). A correlation analysis was thereafter performed, by computing the Pearson R coefficient, defined as:

$$R = \frac{\Sigma\left(B_i - \overline{B}\right)\left(T_i - \overline{T}\right)}{\sqrt{\Sigma\left(B_i - \overline{B}\right)^2}\sqrt{\Sigma\left(T_i - \overline{T}\right)^2}} \quad (3)$$

where $B_i$ corresponds to the cell count from given BLUE image (ground truth) and $T_i$ the corresponding cell count from TL image.

As *R* can fastly tend to 1 with relatively poor performance, the sum of squared errors (*sse*) was also computed from the linear fit, to obtain a deeper insight into the efficacy of the employed model:

$$sse = \sum (B_i - (\propto + \beta T_i))^2 \quad (4)$$

where $\propto$ and $\beta$ correspond to the coefficients of fitted linear regression curve. The performance of the model increases as the *sse* tends to 0.

### 2.7. Training set preparation for cell classification

Three independent acquisitions of human and mouse cells left untreated as control (CM) or treated with DACT (a well-known transcription inhibitor [4]) for 4 h, were performed using the TL channel, capturing brightfield images. In total, 402 images were acquired and processed as follows (Fig. 3, Fig. 4). First, images were normalized plate-wise according to control pixel percentiles (as previously described) and untiled to generate 256 × 256 pixel blocks (64 patches per image). Nuclear probability maps were generated using the previously-trained UNET model, and full images were reconstructed by tiling probability blocks. A median filter (with a 5-pixel-sized kernel) was then applied to the obtained reconstructed images and subjected to a sigmoid scaling with $\lambda = 0.001$ and $z = 0.6$. Binary masks were thereafter created by thresholding images using Otsu's method and cleaned from noise using a geodesic opening with a disc kernel of 23 pixels. Nuclear objects were finally separated and labeled using a watershed operation. This final step allowed to compute centroid coordinates of each cell, thus enabling the random selection of a maximum of 5000 cells for each class by defining a frame of 121 × 121 pixels around each centroid (corresponding to the approximate maximum area of studied cells). Of note, nuclei with an area higher than 4500 pixels (≈470 μm$^2$) or lower than 1000 pixels (≈104 μm$^2$) were excluded from the selection, in order to limit detection artifacts. In the end, an annotated tensor $t_{cell}(9314, 121, 121, 1)$ composed of 4839 controls (CM) and 4475 DACT-treated cell patches was generated. Details about tensor composition can be consulted in Supplementary Table S5.

### 2.8. DCNN training for cell classification

A VGG16-derived sequential *keras* model was designed as described in Fig. 3B and trained using the previously described input data (split into "training" (80%) and "validation" (20%) sets), using an *Adam optimizer*, with a *binary cross-entropy* (BCE) loss function, and the *accuracy* evaluation metrics. In sum, the trained model was able to calculate the probability vector of belonging to the "DACT-like" class from a cell patch.

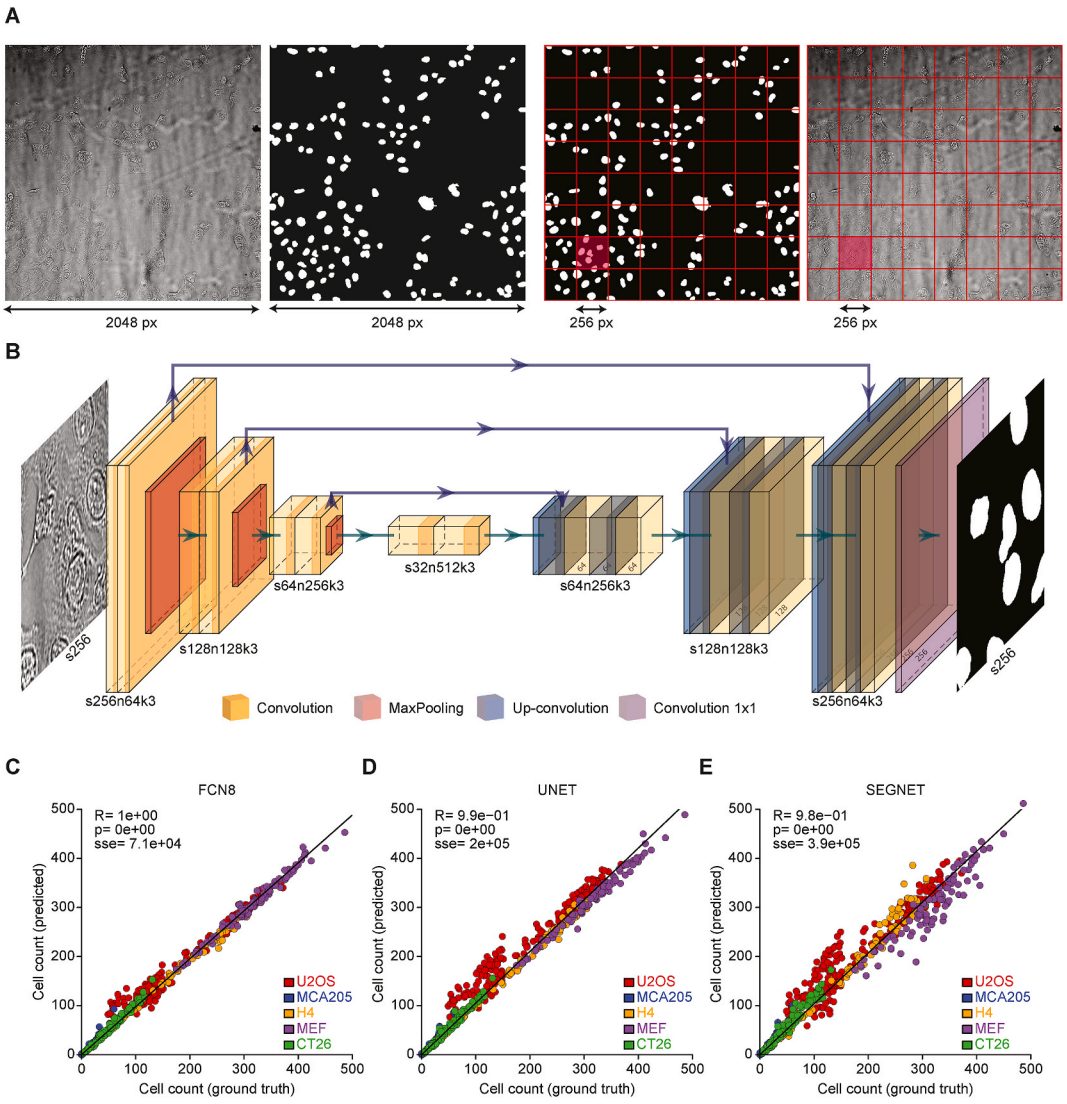


**Fig. 2.** UNET training for label-free nuclei detection. (A) Nuclear masks and normalized brightfield images are split in 256 × 256 pixel blocks and used for training a 3-layer UNET neuronal network, the structure of which is shown in (B). Each step indicates the tensor characteristics (s: size, n: features number, k: kernel size) and the performed operations, as indicated in the legend. (C–E) Model performance was assessed on a testing set including various cell types (as indicated in color legend) by calculating cell count in brightfield images and comparing the obtained result to ground truth, as determined using nuclear staining (D). The UNET model performance was compared to two other widely-used models, namely FCN8 (C) and SEGNET (E). R, Pearson coefficient; p, correlation test p-value; sse, squared estimate of errors.

### 2.9. Cell dynamic transcription inhibition assessment and evaluation

U2OS cells were seeded and treated with either CM, DMSO, DACT, MTX, OXA, CDDP or OL as described above, and imaged every 10 min for 4 h, and then every hour for additional 12 h, using the TL channel (3 viewfields in duplicate wells per condition). Nuclear masks were generated using the trained UNET model, and the total number of viable cells was calculated in all images. Of note, dead cells (characterized by a high refringence in brightfield) were distinguished by measuring the nuclear intensity in TL images from which background was removed using a top-hat filter with a gaussian kernel of 75 pixels. The ratio of "DACT-like" cells was computed timewise on a subsample of 180 cells per condition (30 per image), by determining the number of cells classified as such with a probability $p > 0.5$, applying the trained DCNN model. Time series were compared by means of a paired Mann-Whitney u-test.

### 2.10. Environment

The entire analytic process, including image processing, deep learning and data mining, was performed using R version 3.6.3, on a high-end computer equipped with Intel Xeon E5-2620 v2 CPU, NVIDIA RTX2060 SUPER GPU and 64 GB DDR3 RAM, running under Ubuntu 18.04.

## 3. Results

UNET trained model can accurately detect nuclei from various cell types in brightfield images.

The 3-layer UNET model led to optimal results when it was trained with a batch size of 32 individuals, the evaluation metrics converging for both training and validation sets after 20 epochs. A learning rate of $10^{-4}$ for the *Adam optimizer* was sufficient to avoid model overfitting, as both showed similar final *Dice, accuracy* and *loss* values (training *loss* = 0.22; validation *loss* = 0.27; training *Dice* = 0.84; validation *Dice* = 0.81; training *accuracy* = 0.98, validation *accuracy* = 0.97). The model

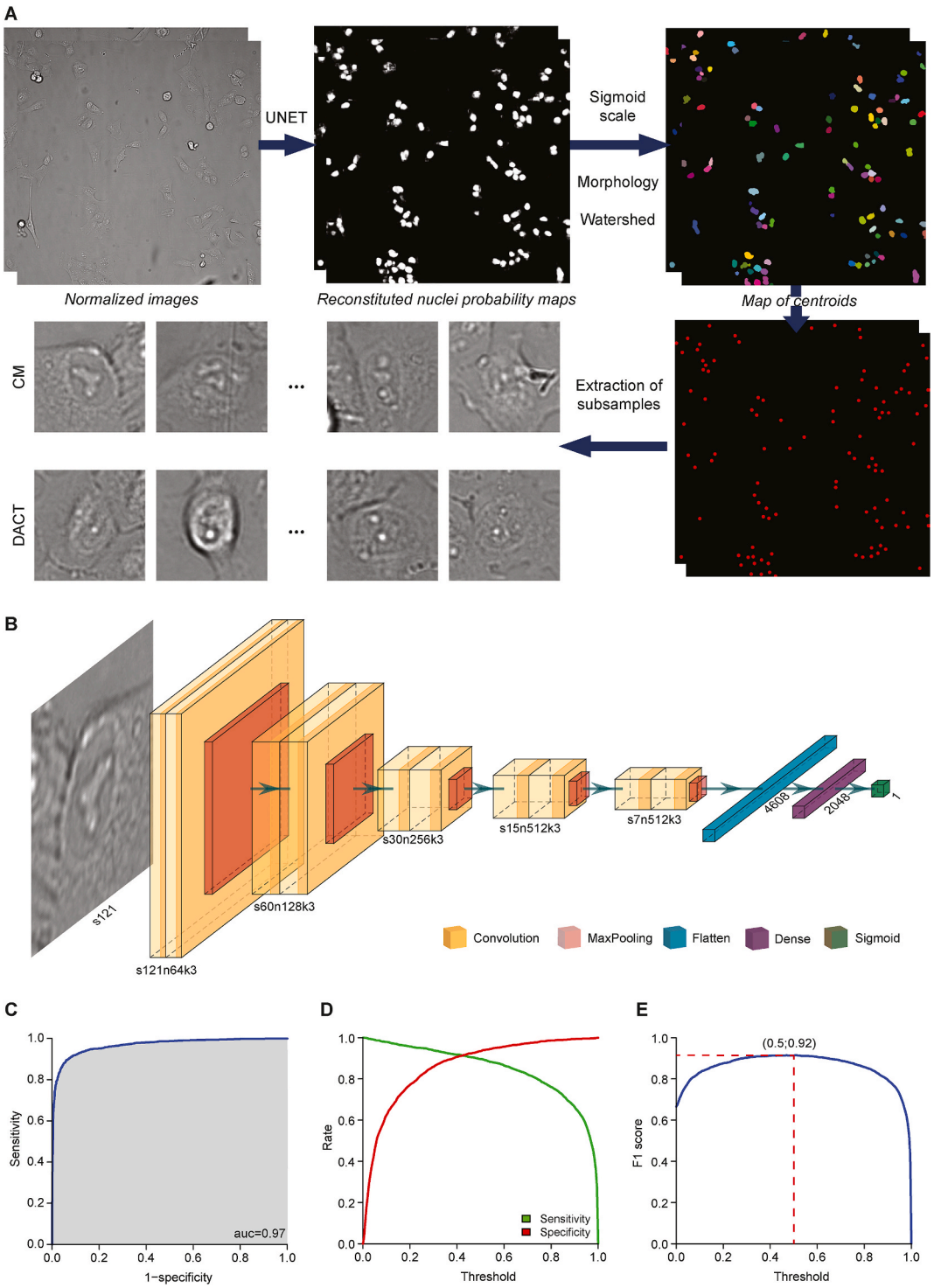


**Fig. 3.** Deep convolutional neural network training for cell classification. Main steps leading to DCNN training are plotted. (A) After automated acquisition of brightfield images, nuclear probability maps are generated by applying the previously trained nuclear detection network. Nuclear masks are thereafter generated and labeled after applying a watershed operation, allowing to compute a map of cellular centroids. A subsample of cellular images is then selected and pooled from these obtained coordinates. (B) Pooled images are annotated as "DACT-like" when relevant and used to train a *keras* sequential convolution model. Each step indicates the tensor characteristics (s: size, n: features number, k: kernel size) and the performed operations, as indicated in the legend. (C, D, E) The model performance was assessed by calculating specificity, sensitivity and F1-score given different applied thresholds.

performance was thereafter evaluated by segmenting test images using both the trained network and conventional image analysis workflow on nuclear stained cells, and comparing the number of obtained nuclei. Correlation analysis yielded an overall Pearson coefficient R = 0.99, proving the efficacy of the model (Fig. 2D). Interestingly, the validation split ratio (initially set to 0.8/0.2) did not have a major impact on model performance, while switching from a patch-wise to an image-wise split slightly increased segmentation efficacy (Figs. S1 and S2). In order to evaluate whether the UNET architecture was an optimal choice, we compared its performance with two other wide-spread segmentation

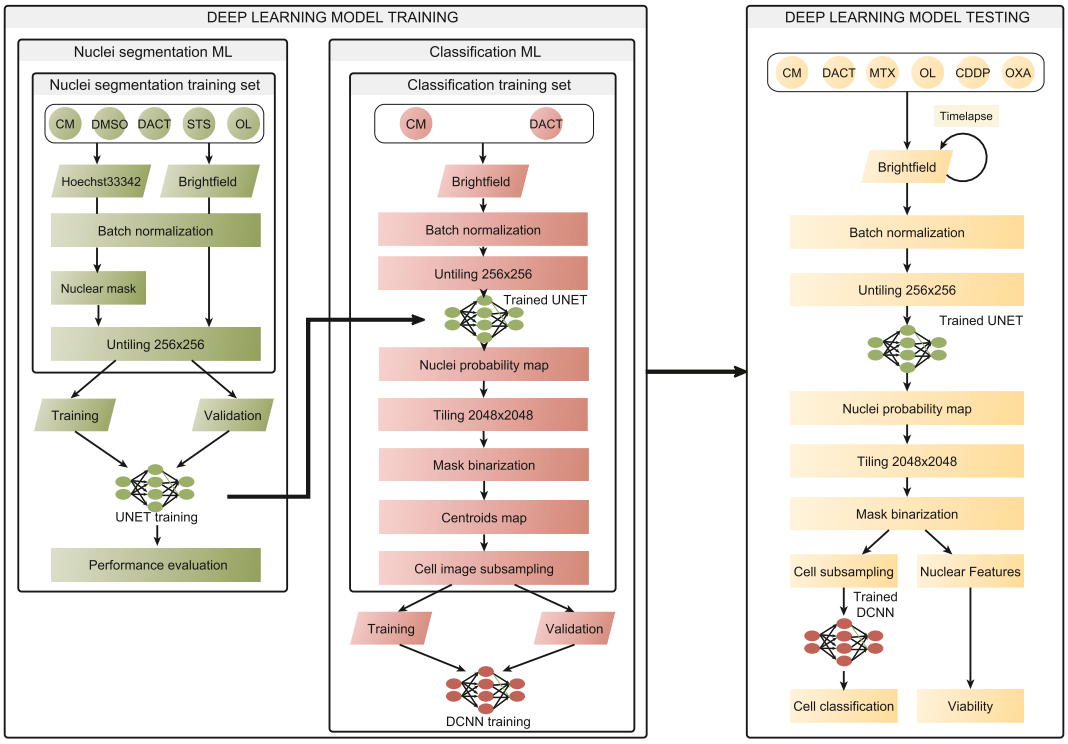


**Fig. 4.** Double deep neural network training and validation for cell classification. Necessary steps required for creating an efficient cell classifier are reported in a flowchart. The network training consists in two successive steps: (1) a UNET architecture training allowing to detect cell nuclei in brightfield images (in green), followed by (2) a sequential DCNN training using annotated single-cell images (in red). The obtained models are thereafter validated by evaluating the proportion of DACT-like cells and their viability in a time-lapse experiment, after treatment with well-known stress inducers (in yellow).

models, FCN8 and SEGNET. The 3 networks showed similar efficacy in detecting nuclei (Fig. 2C, D, E), even if FCN8 was performing slightly better (sse = 7.1e04) than SEGNET (sse = 3.9e05) and UNET (sse = 2e05). Overall, these results suggest that UNET is a reasonable choice over FCN8, the latter being more resource-demanding for computation. Satisfactory results allowing an accurate detection of nuclear high-probability regions in brightfield images were reached, independently of the cell type that was examined.

### 3.1. *DCNN trained model is able to detect transcription inhibition from brightfield images*

The sequential DCNN did not yield any conclusive result when trained on pooled data, including images from either mouse and human cells. As human cancer cell lines are the most prominent models used in cancer research (especially U2OS osteosarcoma cells due to their strong adherence, fast growth and transfection efficiency), we decided to focus on human H4 and U2OS cell lines. The sequential DCNN was trained using 20 epochs with a batch size of 256 individuals, leading to a non-overfitted model confirmed by a similar convergence for both training and validation sets (training *loss* = 0.21; training *binary accuracy* = 0.92; validation *loss* = 0.29; validation *binary accuracy* = 0.89). The model performance was evaluated by means of ROC-AUC analysis, leading to an overall area under curve (auc) of 0.97 (Fig. 3C), revealing the efficacy of the model. Furthermore, the F1-score, which corresponds to the harmonic mean of precision and sensitivity, was calculated for various thresholds, leading to a maximum of 0.92 for a threshold of 0.5 (Fig. 3E). This value was selected as the optimal cut-off for subsequent analyses.

### 3.2. *Immunogenic cell death inducers specifically inhibit transcription*

Approximately 95% of U2OS cells were recognized as "DACT-like" cells after 4 h of culture in the presence of two positive controls, namely, DACT-itself and MTX, an anthracene that is known to inhibit DNA-to-RNA transcription as well [6,25] (Fig.5A, C). Of note, these two ICD inducers showed similar effects on cell growth, both reducing the number of viable cells by ~40% after 16 h of treatment (Fig. 5B). OXA, another ICD stimulatory drug [26–28] also inhibited transcription, as indicated by the fact that more than ~90% of cells were classified as "DACT-like" after 4 h. Interestingly, in contrast to DACT and MTX that caused an early effect (starting after 30 min of treatment, to reach a *plateau* after 2.5 h), OXA induced the "DACT-like" phenotype in a delayed fashion (starting at 1 h of treatment). Such a difference could be linked to its moderate effect on cell viability. Indeed, at the concentrations that we used, OXA was cytostatic rather than cytotoxic. In sharp contrast, CDDP, a platinum salt structurally close to OXA but unable to induce ICD [29,30], did not induce the "DACT-like" phenotype when employed at a cytostatic concentration. Still, when using a higher CDDP concentration, a delayed and partial effect was detectable, as previously reported [6]. Such partial effect of CDDP could be explained by its mode of action which differs from the one of DACT. DACT inhibits polymerase progression by stabilizing covalent DNA-topoisomerase-I complexes, whereas CDDP forms adducts with DNA that can be removed by the nucleotide excision repair machinery [31]. Oleate, a fatty acid known to induce an integrated stress response while inhibiting protein secretion at the level of the Golgi apparatus [32,33], failed to affect RNA transcription, even in conditions where cell viability was reduced by ~20% (probably explaining the statistical significance when tested against CM). Altogether, these results confirm and refine the hypothesis that ICD inducers display uncorrelated biological effects, *i.e.* reduction of cell viability and inhibition of DNA-to-RNA transcription, thus validating the dual deep-learning model developed here.

## 4. Conclusion

The present study documents a novel method based on a dual deep-

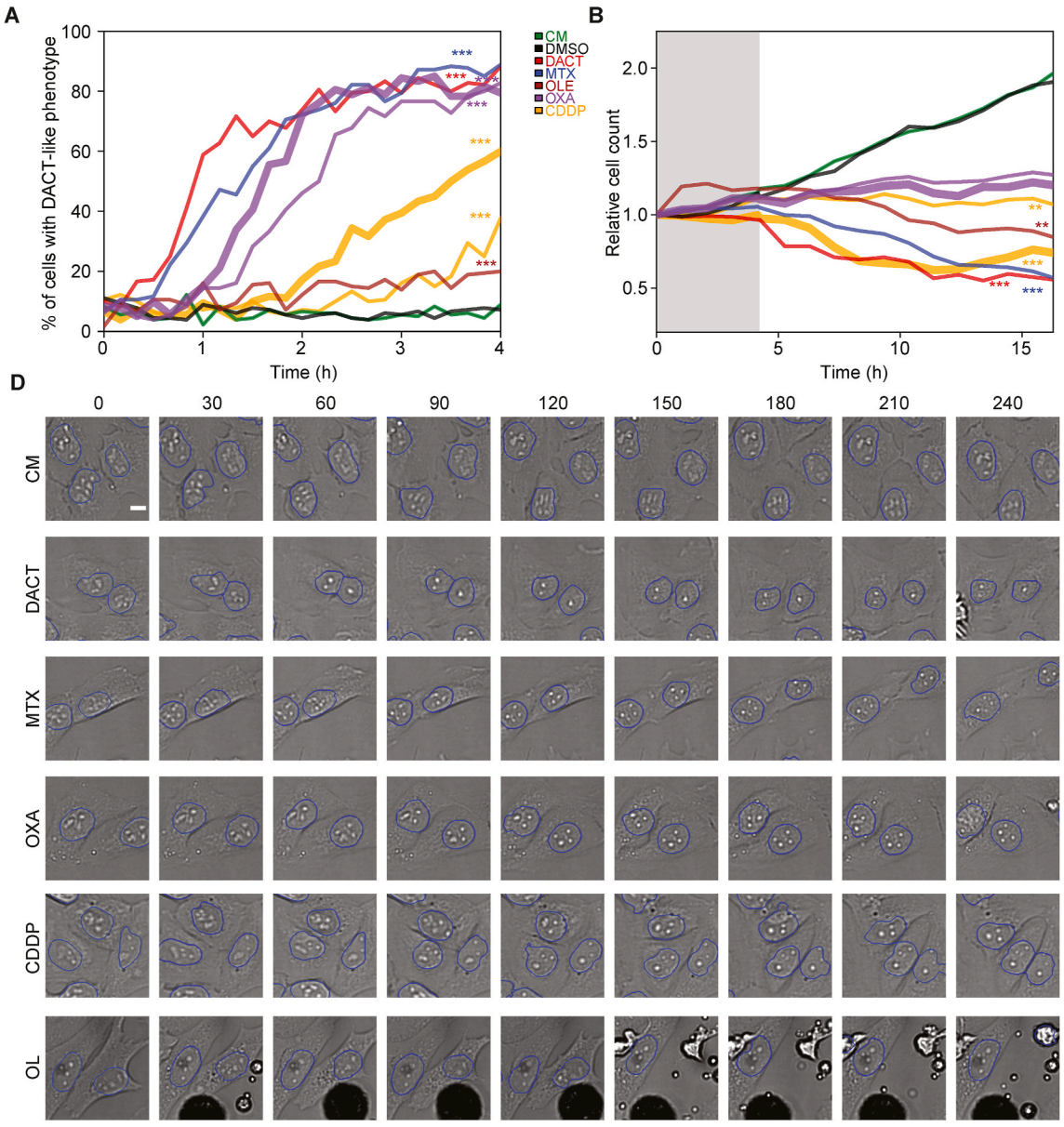


**Fig. 5.** Transcription and viability kinetics assessment in cancer cells using trained double deep neural network. (A–C) Cells were seeded in black-imaging plates, let adapt for 24 h, and were then treated with complete medium (CM, in green) as a control, the solvent 0.1% dimethylsulfoxyde (DMSO, in black), 1 μM dactinomycin (DACT, in red), 4 μM mitoxantrone (MTX, in blue), 500 μM oleate (OL, in brown), 150 and 500 μM oxaliplatin (OXA, in purple, where the thicker line represents the higher concentration), or 150 and 500 μM cisplatin (CDDP, in yellow), and immediately subjected to videomicroscopic observation for 16 h. Brightfield images were taken every 10 min between 0 and 4 h and then every hour between 4 and 16 h. Cellular nuclei were automatically detected using trained UNET, subsampled and then classified using trained DCNN as "DACT-like", the percentage of which was reported in a plot (A). Alternatively, the relative number cells (after exclusion of apoptotic cells containing nuclei with high intensities) were determined (B). Each time series was compared to CM by means of a Mann-Whitney u-test, and p-values were calculated (*$p < 0.05$, **$p < 0.01$, ***$p < 0.001$). Representative time-lapse images of the observed cells together with nuclear segmentation overlay are shown in (C) where time is indicated in minutes. The scale bar represents 10 μm.

learning process allowing to efficiently identify cells that undergo inhibition of DNA-to-RNA transcription in brightfield images. The main advantage of this method lies in its simple implementation: neither staining nor fluorescent microscopy is necessary, rendering this approach cost-efficient for high-throughput screenings. Moreover, the problem arising from the intrinsic fluorescence of many drugs (which often quench signals from fluorescent biosensors or produce saturation artifacts) can be avoided by label-free brightfield microscopy. Instead of expensive fluorophores, it is recommended to acquire a computer equipped with appropriate hardware (CUDA-enabled GPU, see https://developer.nvidia.com/cuda-gpus), even though the method described here is compatible with the CPU versions of the R *tensorflow* and *keras* packages. Naturally, the compiled models are compatible with any tensorflow-capable language (Python, Matlab), and the implementation of the method is not limited to R.

Even though the constructed model was able to extend our knowledge on the effects of conventional ICD inducers on RNA synthesis and cell death, it could be further enriched and applied to the detection of other cellular phenomena such as the inhibition of RNA-to-protein translation or protein secretion. Of note, the inhibitors employed here (DACT, MTX, OXA and CDDP) specifically suppress class I transcription, which is responsible for ribosomal RNA (rRNA) synthesis [34]. Class I transcription mainly occurs in the nucleolus, while other classes of transcription rather take place in the nucleoplasm, perhaps leading to

different phenotypes [35]. In addition, recent studies showed that the dynamic assessment of chromatin motion was differentially affected when using distinct transcriptional inhibitors [36]. Therefore, a refinement of the classification model might be achieved by investigating class-II or class-III inhibitors (such as α-amanitin which, unlike DACT, increases chromatin motion [36,37]) when training our DCNN model. In addition, as the principal goal of our approach is to identify potential ICD-inducing drug candidates from large compounds collections, it could be used as a validation assay following the selection of candidate agents based on algorithms that explore their molecular structure in relationship to their biological activity. In this area, a viable solution using Quantitative structure-activity relationship (QSAR) allowed to identify *in silico* inhibitors of HDAC1, a protein widely involved in eukaryotic gene regulation [38]. Along similar lines, DNA-binding sites of regulatory proteins were successfully predicted [39], opening further perspectives for drug design.

In addition, the present model, which focuses on an osteosarcoma cell line (and was validated in a neuroglioma cell line, not shown), could be refined and applied to other cell types from different model organisms, on which the detection of nuclei in brightfield images has successfully been performed by means of the UNET trained model or other methods [40]. Finally, the described label-free screening pipeline could be applied to cell biological studies that trespass the realm of ICD.

## Acknowledgments

GK is supported by the Ligue contre le Cancer (équipe labellisée); Agence Nationale de la Recherche (ANR) – Projets blancs; AMMICa US23/CNRS UMS3655; Association pour la recherche sur le cancer (ARC); Association "Ruban Rose"; Cancéropôle Ile-de-France; Fondation pour la Recherche Médicale (FRM); a donation by Elior; Equipex Onco-Pheno-Screen; European Joint Programme on Rare Diseases (EJPRD); Gustave Roussy Odyssea, the European Union Horizon 2020 Projects Oncobiome and Crimson; Fondation Carrefour; High-end Foreign Expert Program in China (GDW20171100085), Institut National du Cancer (INCa); Inserm (HTE); Institut Universitaire de France; LabEx Immuno-Oncology (ANR-18-IDEX-0001); the RHU Torino Lumière; Seerave Foundation; SIRIC Stratified Oncology Cell DNA Repair and Tumor Immune Elimination (SOCRATE); and SIRIC Cancer Research and Personalized Medicine (CARPEM). This study contributes to the IdEx Université de Paris ANR-18-IDEX-0001. GC is supported by a scholarship of the Fondation pour la Recherche Médicale (FDT202001011060). We are grateful to Dr. Frédéric Commandeur and Dr. Diana Deaconu for their review of the manuscript.

## Appendix A. Supplementary data

Supplementary data to this article can be found online at https://doi.org/10.1016/j.compbiomed.2021.104371.

## Author contributions

Conceptualization, G.K., A.S. and J.H.; Methodology, G.K., A.S., G.C. and J.H.; Investigation, G.C., J.H., M.L. and A.S.; Formal Analysis, A.S, G.C. and M.L.; Writing – Original Draft, A.S. and G.K.; Writing –Review & Editing, O.K., G.K.; Funding Acquisition, G.K.; Supervision, G.K.

## Data availability

The R code and datasets related to this article can be found at https://doi.org/10.6084/m9.figshare.c.5205278.v2, an open-source online data repository hosted at figshare (Tim O'Reilly, 2015). The images used for the UNET performance evaluation will be available upon request.

## References

[1] L. Galluzzi, et al., Immunostimulation with chemotherapy in the era of immune checkpoint inhibitors, Nat. Rev. Clin. Oncol. 17 (12) (2020) 725–741.
[2] M. Volkova, R. Russell 3rd, Anthracycline cardiotoxicity: prevalence, pathogenesis and treatment, Curr. Cardiol. Rev. 7 (4) (2011) 214–220.
[3] O. Kepp, et al., Consensus guidelines for the detection of immunogenic cell death, OncoImmunology 3 (9) (2014), e955691.
[4] C. Schofer, et al., Redistribution of ribosomal DNA after blocking of transcription induced by actinomycin D, Chromosome Res. 4 (5) (1996) 384–391.
[5] H.M. Sobell, Actinomycin and DNA transcription, Proc. Natl. Acad. Sci. U. S. A. 82 (16) (1985) 5328–5331.
[6] J. Humeau, et al., Inhibition of transcription by dactinomycin reveals a new characteristic of immunogenic cell stress, EMBO Mol. Med. 12 (5) (2020) e11622.
[7] N. Laham-Karam, et al., Transcription and translation inhibitors in cancer treatment, Front Chem 8 (2020) 276.
[8] A. Sauvat, et al., ColocalizR: an open-source application for cell-based high-throughput colocalization analysis, Comput. Biol. Med. 107 (2019) 227–234.
[9] K.I. Farley, et al., Determinants of mammalian nucleolar architecture, Chromosoma 124 (3) (2015) 323–331.
[10] S. Robertson, et al., Digital image analysis in breast pathology-from image processing techniques to artificial intelligence, Transl. Res. 194 (2018) 19–35.
[11] L.-C. Chen, et al., Rethinking Atrous Convolution for Semantic Image Segmentation, 2017.
[12] L.-C. Chen, et al., DeepLab: semantic image segmentation with deep convolutional nets, atrous convolution, and fully connected CRFs, IEEE Trans. Pattern Anal. Mach. Intell. 40 (4) (2016) 834–848.
[13] J. Redmon, et al., You only look once: unified, real-time object detection, in: 2016 IEEE Conference on Computer Vision and Pattern Recognition (CVPR), 2016.
[14] K. Simonyan, A. Zisserman, Very Deep Convolutional Networks for Large-Scale Image Recognition, arXiv 1409.1556, 2014.
[15] K. Yanagisawa, et al., Convolutional neural network can recognize drug resistance of single cancer cells, Int. J. Mol. Sci. 21 (9) (2020).
[16] O. Ronneberger, P. Fischer, T. Brox, U-Net: Convolutional Networks for Biomedical Image Segmentation, Springer International Publishing, Cham, 2015.
[17] C. Ounkomol, et al., Label-free prediction of three-dimensional fluorescence images from transmitted-light microscopy, Nat. Methods 15 (11) (2018) 917–920.
[18] M.D. Guay, et al., Dense cellular segmentation for EM using 2D-3D neural network ensembles, Sci. Rep. 11 (1) (2021) 2561.
[19] G. Pau, et al., EBImage–an R package for image processing with applications to cellular phenotypes, Bioinformatics 26 (7) (2010) 979–981.
[20] N. Otsu, A threshold selection method from gray-level histograms, N/A 9 (1) (1979) 62–66.
[21] M. Abadi, et al., TensorFlow: a system for large-scale machine learning, in: Proceedings of the 12th USENIX Conference on Operating Systems Design and Implementation, USENIX Association, Savannah, GA, USA, 2016, pp. 265–283.
[22] E. Shelhamer, J. Long, T. Darrell, Fully convolutional networks for semantic segmentation, IEEE Trans. Pattern Anal. Mach. Intell. 39 (4) (2017) 640–651.
[23] V. Badrinarayanan, A. Kendall, R. Cipolla, SegNet: A Deep Convolutional Encoder-Decoder Architecture for Image Segmentation, 2017.
[24] D. Kingma, J. Ba, Adam: a method for stochastic optimization, in: International Conference on Learning Representations, 2014 abs/1412.6980.
[25] M. Obeid, et al., Calreticulin exposure dictates the immunogenicity of cancer cell death, Nat. Med. 13 (1) (2007) 54–61.
[26] A. Tesniere, et al., Immunogenic death of colon cancer cells treated with oxaliplatin, Oncogene 29 (4) (2010) 482–491.
[27] L. Zitvogel, et al., Immunogenic tumor cell death for optimal anticancer therapy: the calreticulin exposure pathway, Clin. Canc. Res. 16 (12) (2010) 3100–3104.
[28] T. Yamazaki, et al., Defective immunogenic cell death of HMGB1-deficient tumors: compensatory therapy with TLR4 agonists, Cell Death Differ. 21 (1) (2014) 69–78.
[29] I. Martins, et al., Restoration of the immunogenicity of cisplatin-induced cancer cell death by endoplasmic reticulum stress, Oncogene 30 (10) (2011) 1147–1158.
[30] P. Liu, et al., Crizotinib-induced immunogenic cell death in non-small cell lung cancer, Nat. Commun. 10 (1) (2019) 1486.
[31] W.H. Ang, M. Myint, S.J. Lippard, Transcription inhibition by platinum-DNA cross-links in live mammalian cells, J. Am. Chem. Soc. 132 (21) (2010) 7429–7435.
[32] A. Sauvat, et al., Trans-fats inhibit autophagy induced by saturated fatty acids, EBioMedicine 30 (2018) 261–272.
[33] G. Cerrato, et al., Oleate-induced aggregation of LC3 at the trans-Golgi network is linked to a protein trafficking blockade, Cell Death Differ. (2020). Epub ahead of print.
[34] K. Burger, et al., Chemotherapeutic drugs inhibit ribosome biogenesis at various levels, J. Biol. Chem. 285 (16) (2010) 12416–12425.
[35] A. Pombo, et al., Regional specialization in human nuclei: visualization of discrete sites of transcription by RNA polymerase III, EMBO J. 18 (8) (1999) 2241–2253.
[36] M. Babokhov, et al., Local chromatin motion and transcription, J. Mol. Biol. 432 (3) (2020) 694–700.
[37] O. Bensaude, Inhibiting eukaryotic transcription: which compound to choose? How to evaluate its activity? Transcription 2 (3) (2011) 103–108.

[38] J. Shi, G. Zhao, Y. Wei, Computational QSAR model combined molecular descriptors and fingerprints to predict HDAC1 inhibitors, Med. Sci. 34 (F1) (2018) 52–58.
[39] Q. Zhang, Z. Shen, D.S. Huang, Predicting in-vitro transcription factor binding sites using DNA sequence + shape, IEEE ACM Trans. Comput. Biol. Bioinf 24 (2019) 154–163.
[40] R. Ali, et al., Automatic segmentation of adherent biological cell boundaries and nuclei from brightfield microscopy images, Mach. Vis. Appl. 23 (4) (2012) 607–621.